

# The Hot and Clumpy Molecular Cocoon Surrounding the Ultracompact H II Region G5.89–0.39

Yu-Nung Su,<sup>1</sup> Sheng-Yuan Liu,<sup>1,2</sup> Kuo-Song Wang,<sup>1</sup> Yi-Hao Chen,<sup>3</sup> and Huei-Ru Chen<sup>1,2</sup>

## ABSTRACT

We present observations of CH<sub>3</sub>CN (12–11) emission at a resolution of  $\sim 2''$  toward the shell-like ultracompact H II region G5.89–0.39 with the Submillimeter Array. The integrated CH<sub>3</sub>CN emission reveals dense and hot molecular cocoon in the periphery of the H II region G5.89–0.39, with a CH<sub>3</sub>CN deficient region roughly centered at G5.89–0.39. By analyzing the CH<sub>3</sub>CN emission using population diagram analysis, we find, for the first time, a decreasing temperature structure from 150 to 40 K with the projected distance from Feldt’s star, which is thought to be responsible for powering the H II region. Our results further indicate that the majority of the heating energy in the observed dense gas is supplied by the Feldt’s star. From the derived CH<sub>3</sub>CN column density profile, we conclude that the dense gas is not uniformly-distributed but centrally-concentrated, with a power-law exponent of 5.5 for  $r \lesssim 8000$  AU, and 2.0 for  $8000 \text{ AU} \lesssim r \lesssim 20000$  AU, where  $r$  is the distance to Feldt’s star. The estimated large power index of 5.5 can be attributed to an enhancement of CH<sub>3</sub>CN abundance in the close vicinity of Feldt’s star.

*Subject headings:* H II regions — ISM: individual (G5.89–0.39) — ISM: clouds — stars: formation

## 1. Introduction

G5.89–0.39 (hereafter G5.89, also known as W28 A2) is a shell-like ultracompact (UC) H II region with an angular diameter of  $\sim 4''$ , presumably powered by a young O-type star

---

<sup>1</sup>Institute of Astronomy and Astrophysics, Academia Sinica, P.O. Box 23-141, Taipei 106, Taiwan; ynsu@asiaa.sinica.edu.tw

<sup>2</sup>Institute of Astronomy and Department of Physics, National Tsing Hua University, Hsinchu, Taiwan

<sup>3</sup>Department of Physics, National Taiwan University, Taipei, Taiwan

(Wood & Churchwell 1989). Recently, near-IR observations reported a candidate for powering the UC H II region, an O5-V type star (Feldt et al. 2003, hereafter Feldt’s star), although there is a positional offset of  $\sim 1''$  between the H II region center and the near-IR source. The off-center location probably results from the migration of Feldt’s star (Feldt et al. 2003). The estimated distance to G5.89 varies from 1.9 kpc to 3.8 kpc (Hunter et al. 2008, and references therein). In this letter, we adopt a distance of 2 kpc, which is favored by most recent studies (e.g., Watson et al. 2007; Hunter et al. 2008). Several signposts of high-mass star formation such as energetic outflows (e.g., Sollins et al. 2004; Watson et al. 2007; Hunter et al. 2008) and maser activities (Fish et al. 2005; Kurtz et al. 2004) have been reported toward this region. The orientation of the reported outflows in various tracers is notably different, indicating the existence of multiple young stellar objects in this region (Hunter et al. 2008, and reference therein). Indeed, subarcsecond sub-millimeter observations have identified at least five dust condensations (denoted as SMA1, SMA2, SMA-N, SMA-E and SMA-S) (Hunter et al. 2008). With the existence of a young O-type star still embedded in its natal cloud core, G5.89 provides an ideal laboratory for studying the physical and chemical conditions of molecular gas surrounding a newly formed massive star.

In this letter, we present methyl cyanide ( $\text{CH}_3\text{CN}$ ) observations of G5.89 at an angular resolution of  $\sim 2''$  with the Submillimeter Array<sup>1</sup> (SMA). As  $\text{CH}_3\text{CN}$  is a symmetric-top molecule, its  $K$ -ladder components between adjacent  $J$  levels are closely spaced in frequency while dramatically different in excitation energies. Therefore, an excitation analysis of the  $\text{CH}_3\text{CN}$   $K$ -ladder transitions provides an ideal tool for probing (rotational) temperature of dense molecular gas with small calibration uncertainties (Cummins et al. 1983). Since radiative transitions are not allowed across  $K$ -ladders, the derived rotational temperature is close to the kinetic temperature if the gas is thermalized. Using population diagram (PD) analysis (Goldsmith & Langer 1999), we derive the distribution of the temperatures as well as the filling factor and column density of  $\text{CH}_3\text{CN}$  gas toward G5.89. We then discuss the implications of the observed temperature, filling factor and  $\text{CH}_3\text{CN}$  column density structures and evaluate the density profile in this region. A possible variation of  $\text{CH}_3\text{CN}$  fractional abundance is also illustrated.

---

<sup>1</sup>The Submillimeter Array is a joint project between the Smithsonian Astrophysical Observatory and the Academia Sinica Institute of Astronomy and Astrophysics, and is funded by the Smithsonian Institution and the Academia Sinica.

## 2. Observations and Data Reduction

The observations of CH<sub>3</sub>CN (12–11) in the band of 220 GHz were carried out with the SMA on 2008 April 17 and May 2. With seven antennas in the array, the projected baselines ranged from about 9 m to 120 m (7 to 90 kλ). The phase center was R.A. = 18<sup>h</sup>00<sup>m</sup>30.32<sup>s</sup> (J2000) and decl. = –24°04′00.50″ (J2000), and the half-power width of the SMA primary beam was ~54″. The spectral resolution was 0.41 MHz, corresponding to a velocity resolution of ~0.55 km s<sup>–1</sup>. The total available double-sideband bandwidth was 4 GHz. See Ho, Moran, & Lo (2004) for more complete specifications of the SMA. The flux calibrators were Uranus (Apr 17) and Titan (May 2), and the bandpass calibrators were 3C273 (Apr 17 and May 2) and 3C454.3 (Apr 17). The nearby compact radio sources 1733–130 ( $S \sim 2.8$  Jy in both Apr 17 and May 2) and 1924–292 ( $S \sim 4.4$  Jy in Apr 17 and 4.7 Jy in May 2) served as complex gain calibrators. We calibrated the data using the MIR software package and made maps using the MIRIAD package. With uniform weighting, the synthesized beam size was about 3.1″ × 1.8″ at P.A. of 55.0°. The rms noise level in a single channel of the spectral line images was ~130 mJy beam<sup>–1</sup> (equivalently ~0.6 K).

## 3. The Spectra and Morphology of the CH<sub>3</sub>CN Emission

Figure 1 shows the integrated  $K = 3$  component of the CH<sub>3</sub>CN (12–11) transition. Figure 2 shows the CH<sub>3</sub>CN (12–11) spectra toward the five sub-mm dust components identified by Hunter et al. (2008) as well as toward Feldt’s star. The  $K$  components of the CH<sub>3</sub>CN (12–11) transition are detected toward G5.89 up to  $K = 7$  with an excitation energy of ~420 K. Comparing the integrated CH<sub>3</sub>CN flux measured from our SMA observations with the single-dish results (e.g., Pankonin et al. 2001), we estimate that approximately 80% of the CH<sub>3</sub>CN emission is recovered by the SMA observations.

The morphologies of the lower  $K$  (i.e.,  $K = 0, 1$ , and 2) components are similar to that of the  $K = 3$  component shown in Figure 1. A cavity roughly centered at the UC H II region can be discerned. This cavity is spatially coincident with the dust-deficient region reported by Hunter et al. (2008), indicating a deficiency of both molecules and dust grains. With a synthesized beam of 3.1″ × 1.8″, the molecular cocoon seen in the  $K = 3$  component is resolved into at least three peaks, here referred to as N-lobe, E-lobe, and S-lobe, whose locations agree with the sub-mm dust condensations SMA-N, SMA-E, and SMA-S, respectively, as shown in Figure 1. The higher  $K$  (i.e.,  $K = 5, 6$ , and 7) components are mainly concentrated in N-lobe (i.e., the vicinity of SMA-N as well as SMA1) and become much weaker or even undetected toward E-lobe and S-lobe.

## 4. Excitation Analysis of the CH<sub>3</sub>CN Gas

### 4.1. Methodology

Given the fairly strong detection of CH<sub>3</sub>CN transitions toward G5.89, estimates of gas temperature as a function of position are feasible. We first performed Gaussian line-profile fitting to estimate line parameters, including radial velocity, line-width, and integrated intensity, of each  $K$  component at each pixel. By assuming observed transitions to be optically thin and in LTE, we then calculated  $N_u^{\text{obs}}$ , the CH<sub>3</sub>CN column density of the upper level of the transition, from the integrated intensities. For details, see equation (1) in Thompson & MacDonald (1999). Since the inferred gas density of  $\gtrsim 10^6 \text{ cm}^{-3}$  (see §5) is at least a factor of 10 higher than the critical density at the derived gas temperature (Chen et al. 2006), the LTE approximation should be valid.

In the G5.89 region the lower  $K$  components of the CH<sub>3</sub>CN (12–11) emission are apparently optically thick, as shown in Figure 2. Under such conditions, a good estimation of gas rotational temperature is not achievable by using the well-known rotation diagram technique (Hollis 1982; Turner 1991). To remedy this situation, we estimate the gas temperature with the PD analysis instead. The difference between the PD analysis and the rotational diagram analysis is that the former includes two additional correction factors, i.e., the optical depth correction factor  $C_\tau (= \tau/(1-e^{-\tau}))$  and the filling factor  $f (= \Omega_s/\Omega_a)$ , where  $\tau$  is the line opacity,  $\Omega_s$  is the source solid angle, and  $\Omega_a$  is the beam solid angle. Under LTE conditions, the rotational temperatures as well as the filling factors and column densities of CH<sub>3</sub>CN can be determined from the following equation in PD analysis:

$$\ln\left(\frac{\hat{N}_u^{\text{obs}}}{g_u}\right) = \ln\left(\frac{N_{\text{tot}}}{Q(T_{\text{rot}})}\right) - \frac{E_u}{kT_{\text{rot}}} + \ln(f) - \ln(C_\tau) \quad (1)$$

where  $\hat{N}_u^{\text{obs}}$  is the expected upper-state column density of the target molecule incorporating the effects of the line opacity ( $C_\tau$ ) and the beam dilution ( $f$ );  $g_u$  is the degeneracy of upper state;  $N_{\text{tot}}$  is the total column density of the molecule;  $Q(T_{\text{rot}})$  is the dimensionless rotational partition function;  $T_{\text{rot}}$  is the rotational temperature; and  $E_u$  is the upper energy level.

According to equation (1), for a given upper level,  $\hat{N}_u^{\text{obs}}$  can be evaluated from a set of  $N_{\text{tot}}$ ,  $T_{\text{rot}}$ ,  $f$ , and  $C_\tau$ . Since  $C_\tau$  is actually a function of  $N_{\text{tot}}$  and  $T_{\text{rot}}$ , the independent parameters are therefore  $N_{\text{tot}}$ ,  $T_{\text{rot}}$ , and  $f$  only. We calculated  $\hat{N}_u^{\text{obs}}$  for the parameter space of  $T_{\text{rot}} = 10\text{--}300 \text{ K}$ ,  $N_{\text{tot}}$  in the range of  $10^{13}\text{--}10^{18} \text{ cm}^{-2}$ , and  $f$  between 0.01 and 1.0. By

comparing  $\hat{N}_{\text{u}}^{\text{obs}}$  with  $N_{\text{u}}^{\text{obs}}$  deduced from observational results, we performed  $\chi^2$  minimization

$$\chi^2 = \sum \left( \frac{N_{\text{u}}^{\text{obs}} - \hat{N}_{\text{u}}^{\text{obs}}}{\delta N_{\text{u}}^{\text{obs}}} \right)^2 \quad (2)$$

to determine for each pixel the physical properties, i.e.,  $T_{\text{rot}}$ ,  $N_{\text{tot}}$ , and  $f$ , from the selected parameter space.  $\delta N_{\text{u}}^{\text{obs}}$  is the 1- $\sigma$  error of  $N_{\text{u}}^{\text{obs}}$ . See Wang et al. (2009) for a detailed description of the analysis method.

## 4.2. Temperature & Illumination of Molecular Gas

As shown in Figure 3a, we have for the first time resolved the temperature structure of the neutral dense gas in this region with the PD analysis. The inferred  $\text{CH}_3\text{CN}$  gas temperatures range from 40 K to 150 K, in agreement with the single-dish results of 56–75 K (Thompson & MacDonald 1999; Pankonin et al. 2001; Purcell et al. 2006). Among the three  $\text{CH}_3\text{CN}$  lobes, N-lobe is the hottest, E-lobe next, and S-lobe is the coldest. In particular, the  $\text{CH}_3\text{CN}$  gas in the close vicinity of Feldt’s star has the highest temperature within the whole region.

To further explore the role of Feldt’s star in illuminating its surrounding gas, we plot the deduced gas temperature  $T_{\text{rot}}$  versus the projected distance,  $d$ , to Feldt’s star. Indeed, a good correlation between the temperature and the projected distance is revealed in Figure 4a. In contrast, the correlation between  $T_{\text{rot}}$  and  $d$  becomes much more vague when the fiducial center is shifted about  $2''$  in any direction away from Feldt’s star. Together with the sufficient luminosity budget of the O5-type Feldt’s star and the non-detection of other candidate H II region powering stars within  $2''$  from Feldt’s star, we conclude that the majority of the energy for heating the dense gas enshrouding the UC H II region G5.89 comes from Feldt’s star.

A power-law fit to the data indicates that the gas temperature scales as  $T_{\text{rot}} \propto d^{-0.40}$ . Note that the deduced temperature  $T_{\text{rot}}(d)$  is actually a representative or averaged temperature for the gas along the line of sight. We suggest, however, that with a highly centrally-concentrated density distribution as shown in §5, the deduced temperature at small  $d$  is heavily weighted by high density, hence this represents the gas temperature at small  $r$ , where  $r$  is the distance to Feldt’s star. Therefore the temperature profile  $T_{\text{rot}}(d)$  can be viewed as  $T_{\text{rot}}(r)$ . The temperature profile of  $T \propto r^{-0.40}$  is shallower than the profile of  $T \propto r^{-3/4}$  measured toward hot-molecular core sources (e.g., Cesaroni et al. 1998; Beltrán et al. 2005). This disparity can be attributed to different dust grain properties and/or variant evolutionary stages. The temperature structure provides clues for the dust opacity index  $\beta$ . Theoretical models found that, for example, the temperature structure of uniform dust shells

surrounding a newly formed O star can be described by  $T_{dust} \propto r^{-\alpha}$ , where  $\alpha \approx 2/(\beta+4)$  (Wolfire & Churchwell 1994). Modifications of the models with a centrally-concentrated density profile, however, are required to match the case of G5.89.

### 4.3. Filling Factors & Column Density Profiles

Figures 3*b* and 3*c* show the derived filling factor and CH<sub>3</sub>CN column density, respectively. The CH<sub>3</sub>CN column density plotted in Figure 3*c*,  $N_{tot,f=0.1}$ , is the CH<sub>3</sub>CN column density scaled by a filling factor of 0.1 (see below). Figure 4*b* shows the derived filling factor versus the projected distance to Feldt’s star, and it clearly demonstrates that the molecular gas in the close vicinity of Feldt’s star (i.e.,  $d \lesssim 6000$  AU, mainly associated with N-lobe) has small filling factors ranging from 0.02 to 0.24, suggestive of a clumpy medium. The small filling factors can also be readily recognized from the low brightness temperatures ( $\lesssim 20$  K) of the hot ( $\sim 100$ – $150$  K) but optically thick low- $K$  components. For the gas further out, the filling factors become noticeably scattered with not only large values of 0.8–1 for the majority but also large uncertainties. Nevertheless, such large uncertainties in fact imply all the observed transitions to be optically thin. In such case, the filling factor,  $f$ , and the total column density,  $N_{tot}$ , become degenerate in the calculation and hence cannot be well determined.

In short, the CH<sub>3</sub>CN gas toward G5.89 can be coherently considered as clumpy, with  $f \sim 0.1$ – $0.2$ . As shown in Figure 4*c*, we thus plot the CH<sub>3</sub>CN column density scaled by a filling factor of 0.1,  $N_{tot,f=0.1}$ , versus the projected distance to Feldt’s star. Obviously  $N_{tot,f=0.1}$  decreases with increasing projected distance  $d$ , and the ratio between the inner ( $d \sim 4000$  AU) and outer ( $d \sim 18000$  AU) region is more than a factor of 10. Note that if  $N_{tot}$  instead of  $N_{tot,f=0.1}$  is plotted, this ratio will be even larger because the inferred  $f$  is larger for gas further out.

## 5. Density Structure

The deduced CH<sub>3</sub>CN column density profile reflects the density structure of the molecular gas. For simplicity, we assume a spherical cloud core with a power-law density profile,  $n(r) \sim r^{-p}$ , and a constant CH<sub>3</sub>CN fractional abundance  $X(\text{CH}_3\text{CN})$  of  $1 \times 10^{-9}$ , similar to that found in other massive star forming regions (Wilner et al. 1994; Zhang et al. 1998). We further adopt inner and outer boundaries at 4000 and 20000 AU, respectively, based on the size of the UC H II region and the CH<sub>3</sub>CN emission. We then convolve the column

density with a two-dimensional Gaussian beam of  $3.1'' \times 1.8''$ , equivalent to our SMA beam. As shown in Figure 4c, we examine three model column density profiles calculated with power-law indices  $p$  of 0, 2, and 5.5. The adopted values for density at the inner edge are  $3.5 \times 10^7$ ,  $3.5 \times 10^7$ , and  $3.5 \times 10^8 \text{ cm}^{-3}$ , respectively. Obviously, the modeled column density profile of  $p=0$  (i.e., constant density) is too flat to agree with the observational results (i.e.,  $N_{\text{tot},f=0.1}$  profile). Since the  $N_{\text{tot}}$  profile would be even steeper than  $N_{\text{tot},f=0.1}$ , the discrepancy between the profiles of observations and constant density can not be attributed to the adopted constant filling factor of 0.1. The observed  $N_{\text{tot},f=0.1}$  profile can be well represented by the results modeled from a broken power law density distribution, with  $p = 5.5$  for  $r \lesssim 8000 \text{ AU}$  and  $p = 2.0$  for  $8000 \text{ AU} \lesssim r \lesssim 20000 \text{ AU}$ . Note that for the  $p = 2$  profile, the gas density at  $r = 20000 \text{ AU}$  is  $1.4 \times 10^6 \text{ cm}^{-3}$ , more than sufficient to thermalize the observed  $\text{CH}_3\text{CN}$  transitions. We therefore conclude that a centrally-concentrated density distribution is required to interpret the observational column density profile.

Observations of massive star-forming cores indicated that the density power-law indices range from 1 to 2, while theoretical models also predicted similar power-law indices (e.g., Mueller et al. 2002, and reference therein). The density profile of  $n \sim r^{-5.5}$  is significantly steeper than typical cases. Feedback processes such as the expansion of the  $\text{H II}$  region may play a role to steepen the density profile. Since the observed  $\text{CH}_3\text{CN}$  column density depends on the gas density and  $\text{CH}_3\text{CN}$  abundance,  $X(\text{CH}_3\text{CN})$ , the steep  $\text{CH}_3\text{CN}$  column density profile may also be a result of an enhancement of  $\text{CH}_3\text{CN}$  gas due to the evaporation of grain mantles in the inner region, similar to the cases of abundance jump reported by van der Tak et al. (2000).

Finally, we note that the temperatures as well as column densities are estimated simultaneously under the assumption of one isothermal gas component along the line of sight. While the deduced temperature and density structures are in fact not uniform, they form a self-consistent set of solutions. That is, the highly centrally-concentrated  $\text{CH}_3\text{CN}$  density profile supports the temperature profile, which in turn validates the density profile itself. The derived “projected” profile therefore reflects the actual radial-dependent structure. More rigorous radiative transfer calculation that can account for all the involved parameters such as temperature, density, filling factors, and abundance, as well as observations with even higher angular resolutions will be desired to further refine the results.

We thank all SMA staff for their help during these observations. We thank J. Karr for reading the manuscript. S.-Y. L., Y.-N. S., and H.-R. C. thank the National Science Council of Taiwan for support this work through grants NSC 97-2112-M-001-006-MY2 and NSC 97-2112-M-007-006-MY3.

## REFERENCES

- Beltrán, M. T., et al. 2005, *A&A*, 435, 901
- Cesaroni, R., et al. 1998, *A&A*, 331, 709
- Chen, H.-R., et al. 2006, *ApJ*, 639, 975
- Cummins, S. E., et al. 1983, *ApJ*, 266, 331
- Feldt, M., et al. 2003, *ApJ*, 599, L91
- Fish, V. L., et al. 2005, *ApJS*, 160, 220
- Goldsmith, P. F., & Langer, W. D. 1999, *ApJ*, 517, 209
- Ho, P. T. P., Moran, J., & Lo, K. Y. 2004, *ApJ*, 616, L1
- Hollis J. M., 1982, *ApJ*, 260, 159
- Hunter, T. R., et al. 2008, *ApJ*, 680, 1271
- Kurtz, S., Hofner, P., & Álvarez, C. V. 2004, *ApJS*, 155, 149
- Mueller, K. E., et al. 2002, *ApJS*, 143, 469
- Pankonin, V., et al. 2001, *ApJ*, 558, 194
- Purcell, C. R., et al. 2006, *MNRAS*, 367, 553
- Scoville, N. Z., & Kwan, J. 1976, *ApJ*, 206, 718
- Sollins, P. K., et al. 2004, *ApJ*, 616, L35
- Tang, Y.-W., et al. 2009, *ApJ*, 695, 1399
- Thompson, M. A., & MacDonald, G. H. 1999, *A&AS*, 135, 531
- Turner B. E., 1991, *ApJS*, 76, 617
- Wang, K.-S., et al. 2009, *ApJ*, submitted.
- Watson, C., et al. 2007, *ApJ*, 657, 318
- Wilner, D. J., et al. 1994, *ApJ*, 422, 642
- Wolfire, M. G., & Churchwell, E. 1994, *ApJ*, 427, 889



Wood, D. O. S., & Churchwell, E. 1989, ApJS, 69, 831

van der Tak, F. F. S., et al. 2000, A&A, 361, 327

Zhang, Q., et al. 1998, ApJ, 494, 636

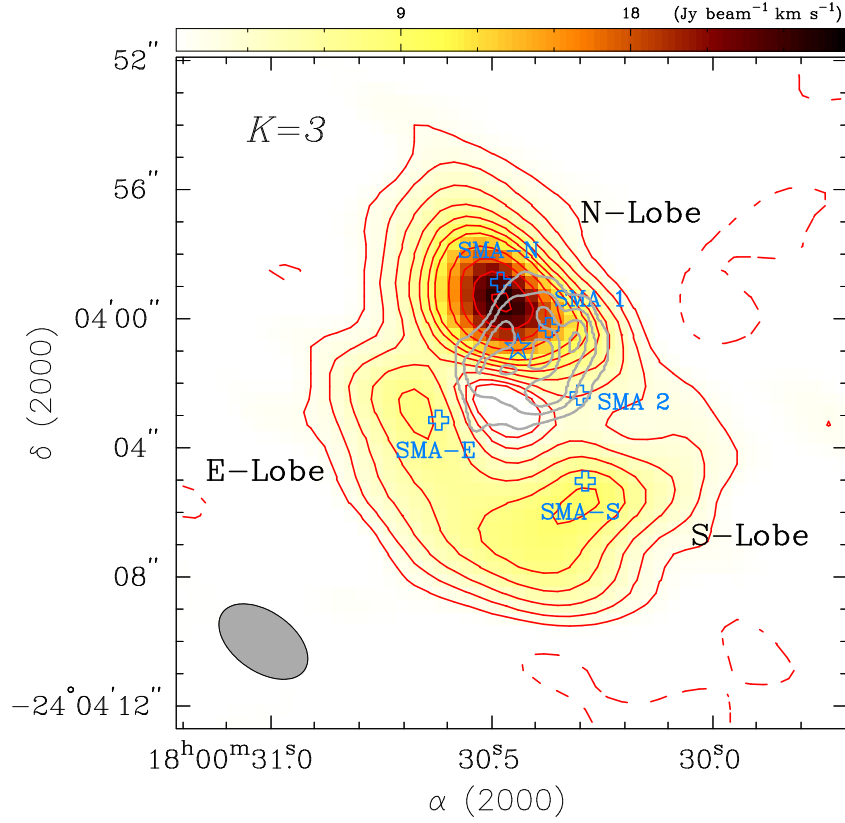


Fig. 1.— The integrated  $K = 3$  component of the  $\text{CH}_3\text{CN}$  (12–11) emission shown in both red contours and color scales. Contour levels are  $-3, 3, 6, 10, 15, 20, 25, 30, 40, 50, 60$ , and  $70 \times 0.35 \text{ Jy beam}^{-1} \text{ km s}^{-1}$ . The gray contours represent the free-free emission at 2 cm (Tang et al. 2009). The dark ellipse at the bottom left denotes the synthesized beam. The crosses mark the positions of the sub-mm dust condensations reported by Hunter et al. (2008) and the star marks the position of Feldt’s star (Feldt et al. 2003).

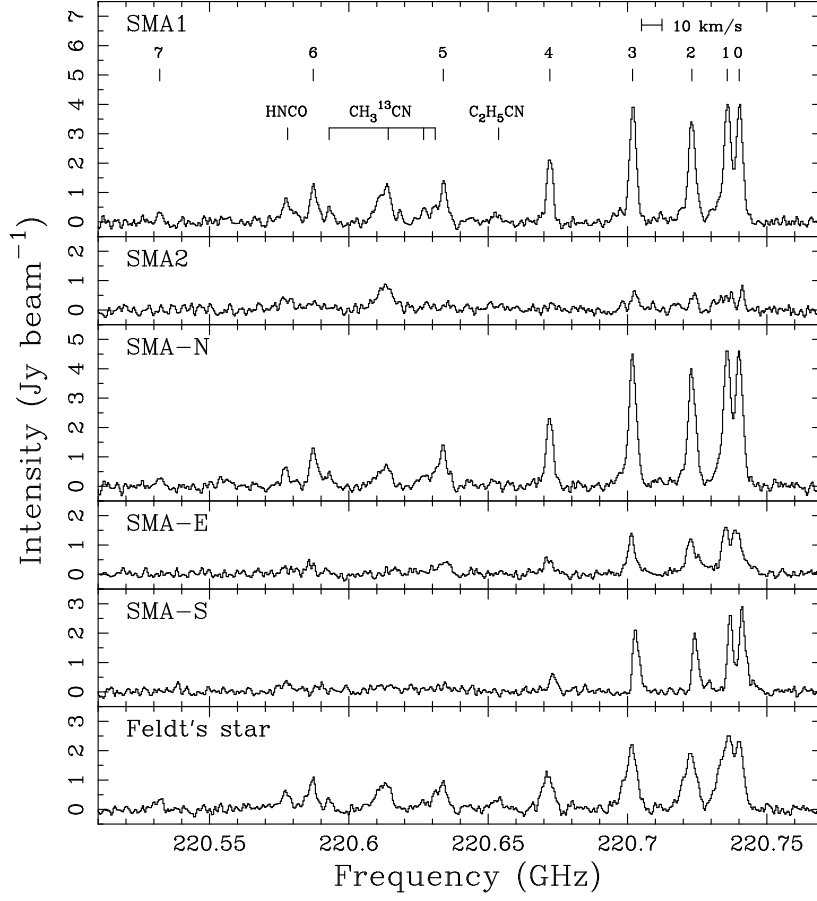


Fig. 2.— The spectra of the  $\text{CH}_3\text{CN}$  (12–11) lines taken at the positions of the five sub-mm dust condensations identified by Hunter et al. (2008) as well as Feldt’s star.

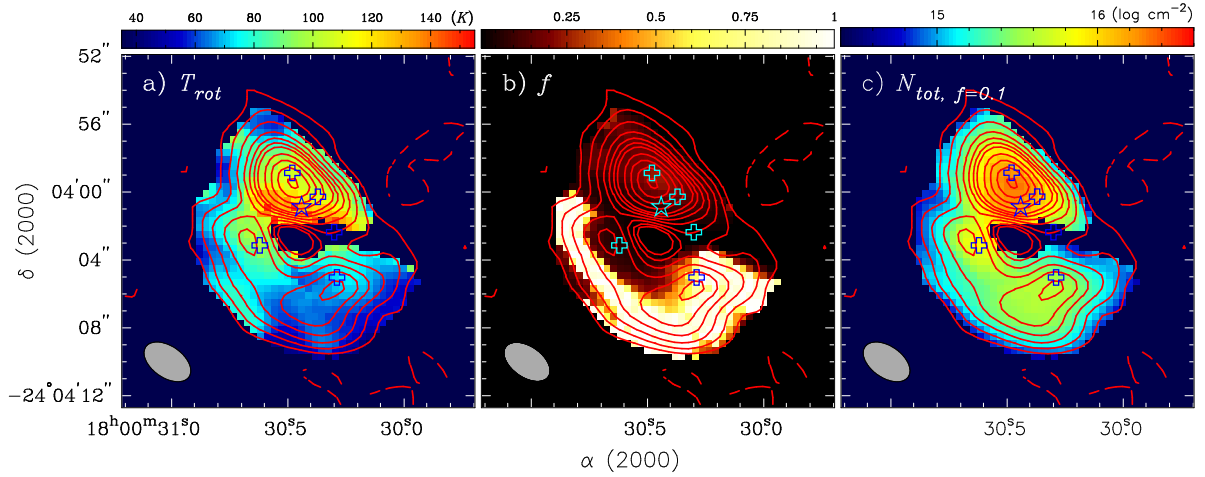


Fig. 3.— The inferred rotational temperature (panel *a*), filling factor (panel *b*), and CH<sub>3</sub>CN column density (panel *c*) in color scales overlaid with the contours of the integrated CH<sub>3</sub>CN (12–11)  $K = 3$  component. The CH<sub>3</sub>CN column density plotted in panel *c*,  $N_{tot, f=0.1}$ , is the CH<sub>3</sub>CN column density scaled by a filling factor of 0.1. Caption as in Figure 1.

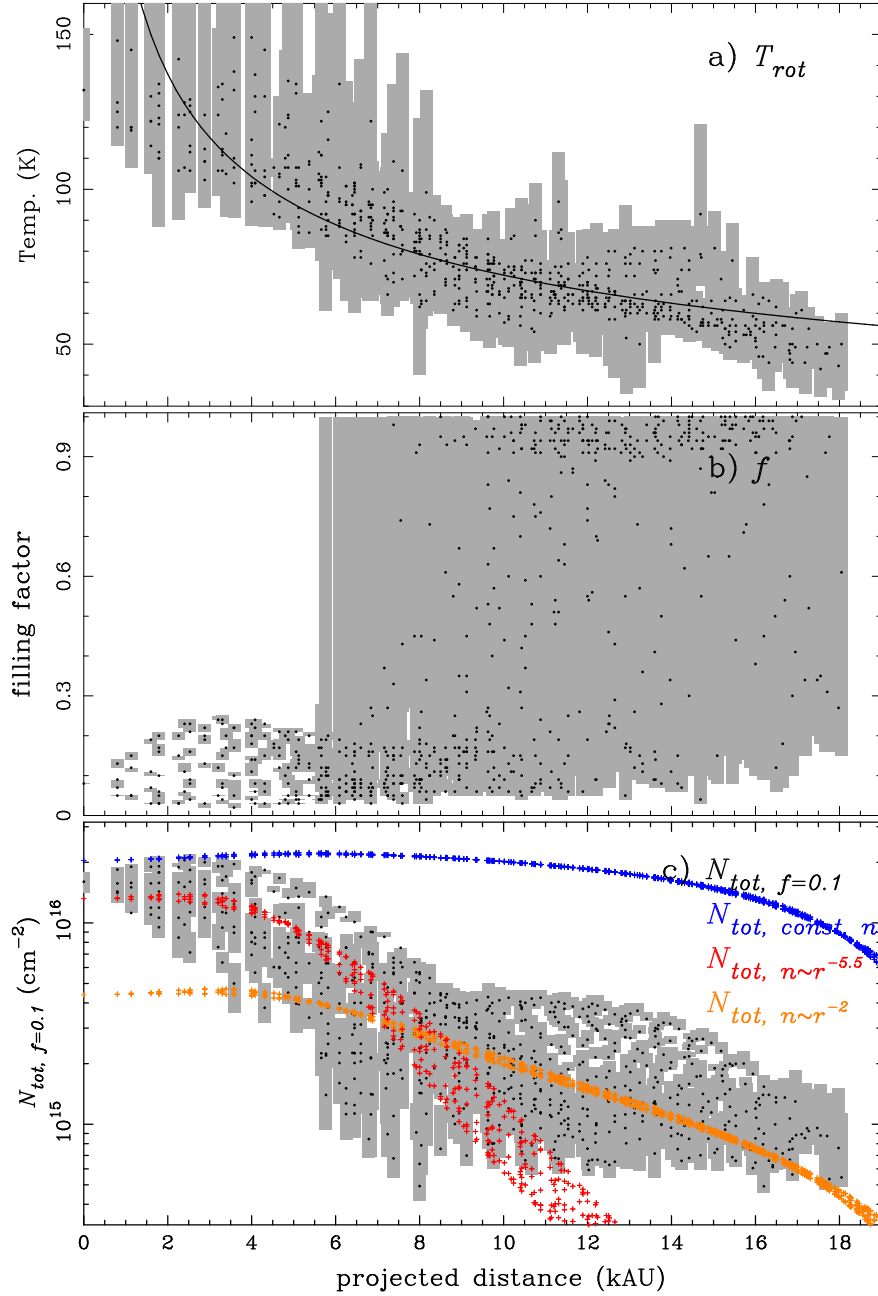


Fig. 4.— The inferred rotational temperature (panel *a*), filling factor (panel *b*), and CH<sub>3</sub>CN column density (panel *c*) versus the projected distance,  $d$ , to the Feldt’s star. In each panel, the overlaid greyscales represent the 1- $\sigma$  error in y-axis of the plotted data. In panel *a*, the best power-law fit,  $T_{\text{rot}} \propto d^{-0.40}$ , is also plotted. In panel *c*, the blue, orange, and red crosses represent the modeled CH<sub>3</sub>CN column densities with the spherical density distributions of power-law indices,  $p$ , of 0, 2, and 5.5. See §5 for the details.